



# Site effect estimation in the Tehran basin and its impact on simulation results

Reza Alikhanzadeh · Hamid Zafarani ·  
Behzad Hassani

Received: 12 February 2023 / Accepted: 5 May 2023 / Published online: 31 May 2023  
© The Author(s), under exclusive licence to Springer Nature B.V. 2023

**Abstract** Recent earthquake damage distributions have demonstrated that the influence of local geology on ground shaking is a significant factor in engineering seismology. So, calculating the site effect is a priority to get a trustworthy assessment of the seismic risk for a location, in addition to studying the local seismic sources. The signal amplitude can be amplified by this effect throughout a range of periods. The site effect has been calculated using a variety of computational and experimental techniques, such as seismic noise measurements. In this study, to calculate the site effect, the analysis of accelerograms recorded by Iran's strong motion network of the Road, Housing, and Urban Development Research Center was used. Here, 294 records from 63 stations were used to calculate the H/V (horizontal to vertical spectral ratio) curve as well as the near-surface high-frequency attenuation parameter ( $\kappa_0$ ). The classification method is based on determining the peak period at each station. To examine site effect consideration, we use the hybrid method composed of the finite difference method

for low frequencies ( $<1$  Hz) and a stochastic finite fault method for high-frequency radiation ( $>1$  Hz) to simulate an earthquake scenario on the Niavaran fault, which is located north of Tehran, Iran. According to the findings, different site classes cause spectral amplitude variations ranging from 11 to 28% at different periods ( $T=0.2, 0.5, 1.0, \text{ and } 4.0$  s).

**Keywords** Site effect · Accelerogram · Inelastic attenuation factor · Near-surface attenuation · Tehran

## 1 Introduction

Recent earthquake damage distributions have demonstrated that the influence of local geology on ground shaking is a significant factor in engineering seismology. Different factors may influence how the Earth's structure beneath the site affects ground motion (e.g., Safak 2001). The impedance contrast between the bedrock and the soft sedimentary cover is, in general, the main factor. The strength of the multi-reflection of waves at particular frequencies within the soft layer, which traps the wave energy within the layer, depends on the impedance contrast. Hence, calculating site effects is a priority to get a trustworthy assessment of the seismic hazard risk for a location, in addition to studying the local seismic source. The signal amplitude can be amplified or de-amplified by site effects throughout a range of periods. To categorize the type of site in building codes like the Iranian seismic

---

R. Alikhanzadeh (✉) · H. Zafarani  
International Institute of Earthquake Engineering  
and Seismology (IIIES), No. 26, Arghavan St., North  
Dibajee, Farmanieh, P.O. Box, Tehran 19395-3913, Iran  
e-mail: reza.alikhan.zadeh@stu.iiies.ac.ir

H. Zafarani  
e-mail: h.zafarani@iiies.ac.ir

B. Hassani  
BC Hydro, Burnaby, Canada  
e-mail: behzad.hassani@bchydro.com

design code (Standard No. 2800), surface geology, or time-averaged shear wave velocity in the first 30 m ( $V_{s30}$ ) are frequently used (Table 1). But the amplitude of the incoming seismic waves can be affected by much deeper layers than 30 m (up to 100 to 200 m, e.g., Lee et al. 1995).

Depending on the geometry and impedance contrast of the ground structure, site effects can vary from simple one-dimensional effects to complex three-dimensional effects. Only a few selected areas, such as the Los Angeles Basin and the Ashigara Valleys, where 3D geo-structural data has been collected, allow for the calculation of such effects (e.g., Olsen and Archuleta 1996; Pitarka et al. 1994). However, even at these places, the predicted basin response has a maximum frequency of around 5 Hz, which is related to how well the geological structure is understood over wavelengths of a few hundred meters (Fukushima et al. 2007; Zhifeng 2022). In some cases, one-dimensional multiple reflection theory calculations can be used to approximate the theoretical site amplification. But at every location, the expense of a deep borehole that reaches the bedrock could be significant. In the United States, an alternate metric for classifying soil conditions is the time-averaged shear wave velocity in the first 30 m (Table 2).  $V_{s30}$  can offer more information than surficial geology data as the impedance effects up to a depth of 30 m

are implicitly taken into account by  $V_{s30}$ . However, to properly estimate the site response for a given site at different periods, a velocity profile that goes well beyond 30 m to the bedrock level should be developed and used to estimate the transfer function.

An alternate site classification system based on the site dominant period was first proposed by Kanai and Tanaka, (1961). The seismic design code for highway bridges in Japan uses this method, which is also described in Table 2. This classification uses a mix of  $V_{s30}$  and the depth of the soil layers rather than precisely following the  $V_{s30}$  method. In this way, deep geological profiles and high shear wave velocities are mapped to the resonance frequency, which is one benefit of this classification. A study using data from Japan (Zhao et al. 2006) recommended four kinds of sites using this method. Since deep soil layers overlying hard rock amplify long-period motions, these authors chose this site classification over the conventional description based on  $V_{s30}$ . In contrast, short periods are amplified by thin, soft soil layers. As  $V_{s30}$  only reflects the shallowest portion of the geological profile, it may not necessarily indicate the natural period of the site. There are two benefits using a classification system based on the dominant period. The first is that the predicted ground motion amplitudes would include both deep geological effects as well as the

**Table 1** Site categories in the Iranian code of practice for the standard seismic resistant design of buildings, Standard No. 2800 (Building and Housing Research Center 2014)

Group	Constituent materials	$V_{s30}$
I	Igneous rocks, hard and stiff sedimentary rocks, and massive metamorphic rocks Conglomerate beds, stiff soil with over 30 m in thickness	$V_{s30} > 750$
II	Loose igneous rocks, friable sedimentary rocks, foliated metamorphic rocks, and Stiff soil with a thickness of less than 30 m	$375 < V_{s30} < 750$
III	Rocks disintegrated by weathering, medium compaction soils, beds of gravel, and sand with medium intragranular cementation bonds	$175 < V_{s30} < 375$
IV	Soft and wet deposits resulted from high levels of water table, any kind of soil containing a 6-m high clay layer less than 175 with a cementation index over 20	$V_{s30} < 175$

**Table 2** Site classification based on JRA, 1980 and its approximate equivalent in NEHRP site classification (BSSC 2000)

Site classes	Site natural period (s)	$V_{s30}$	NEHRP class
SC-I	$T < 0.2$ s	$V_{s30} > 600$ m/s	A + B
SC-II	$0.2 \text{ s} \leq T < 0.4$ s	$300 \text{ m/s} \leq V_{s30} < 600 \text{ m/s}$	C
SC-III	$0.4 \text{ s} \leq T < 0.6$ s	$200 \text{ m/s} \leq V_{s30} < 300 \text{ m/s}$	D
SC-IV	$T \geq 0.6$ s	$V_{s30} < 200 \text{ m/s}$	E

site's whole frequency content. In addition, measurements of ambient noise or H/V spectral ratios on earthquake data can be used at several locations to determine the site's dominant period (e.g., Bonnefoy-Claudet et al. 2006). Additionally, Lusou et al. (2001) demonstrated that site classification using a combination of the dominant period  $V_{s30}$  and H/V decreased the standard deviation of the predicted motions when constructing empirical ground-motion prediction relationships for K-net data. Using average H/V response spectral ratios to categorize K-net sites, Zhao et al. (2006) accurately predicted local site effects while simultaneously lowering the model uncertainty. This method may be used with data categorized into generic categories like rock or soil. The H/V approach has grown in popularity despite being dependent on several assumptions because of how straightforward it is. This approach was used by Lermo and Chavez-Garcia (1993) to analyze earthquake shear wave recordings. Then, Yamazaki and Ansary (1997) expanded this strategy to employ strong seismic acceleration data for various purposes, such as to assess contributing factors to site effects or site categorization. H/V has garnered a lot of interest since it is affordable, does not require a ground velocity model, and can be used for both minor and major earthquakes with only one seismograph. In the current investigation, the seismographic stations were categorized based on the dominant period using the H/V ratio (Yamazaki and Ansary 1997).

According to the technical literature (Beresnev and Atkinson 1997 and its references), site effect estimates must take into account near-surface high-frequency attenuation effects. Also, the characterization of high-frequency attenuation of acceleration ground motion has become an important component of site-specific seismic hazard studies in recent years (e.g., Rodriguez-Marek et al. 2014; Bard et al. 2019). The ground acceleration spectrum at high frequencies diminishes exponentially with frequency, according to the approach of Anderson and Hough (1984) (AH84):

$$A(f, t) = A_0 e^{-\pi f \kappa} \quad (1)$$

Here,  $\kappa$  is estimated from the high-frequency part of the S-wave spectral acceleration domain above a

certain corner frequency where the spectrum begins to decay rapidly ( $f_{\max}$ ) to the noise floor.

The AH84 technique uses this parameter as an arbitrary function of distance and proposes a linear relationship between kappa and epicentral distance ( $R_e$ ):

$$\kappa = \kappa_0 + \kappa_R R_e \quad (2)$$

in such a way that the distribution of  $\kappa$  tends towards limited values ( $\kappa_0$ , near-surface high-frequency attenuation parameter) as  $R_e$  approaches zero, which is commonly considered as site effects.

## 2 Tehran basin

Each of the numerous tectonic regions that make up the Iranian plateau has unique seismic, structural, and geodynamic properties. As a result, determining region-specific ground-motion attenuation is crucial for understanding seismic hazards in Iran. For instance, Motaghi and Ghods (2012) investigated how attenuation parameters varied throughout the central Alborz Mountains. Zafarani et al. (2012) used generalized inversion of the S-wave amplitude spectra to estimate simultaneously source parameters, site response, and S-wave attenuation in northern Iran. Alborz region is a seismotectonic province in northern Iran (Berberian 1976) that is very important from the seismological aspect due to the occurrence of large historical earthquakes and also for its geographical location hosting important cities of Iran, including Tehran as one of the world's largest cities. The majority of the nation's economic, social, industrial, and political infrastructure has congregated in Tehran as a result of the city's growth by several million residents and its growing importance as the nation's capital.

Tehran covering an area of 1274 km<sup>2</sup> at the southern foot of the central Alborz Mountains (Fig. 1), had a population of about 8.7 million in the 2016 census (Statistical Center of Iran [SCI], 2016). The megacity has historical earthquakes of large magnitude (pre-1900) and is surrounded by several active faults in the north, south, east, southeast, and northwest, including faults in the inner city. The seismic risk has significantly increased due to Tehran's rapid urban growth since the 1980s. The likelihood of large-magnitude earthquakes in the city causing significant loss of

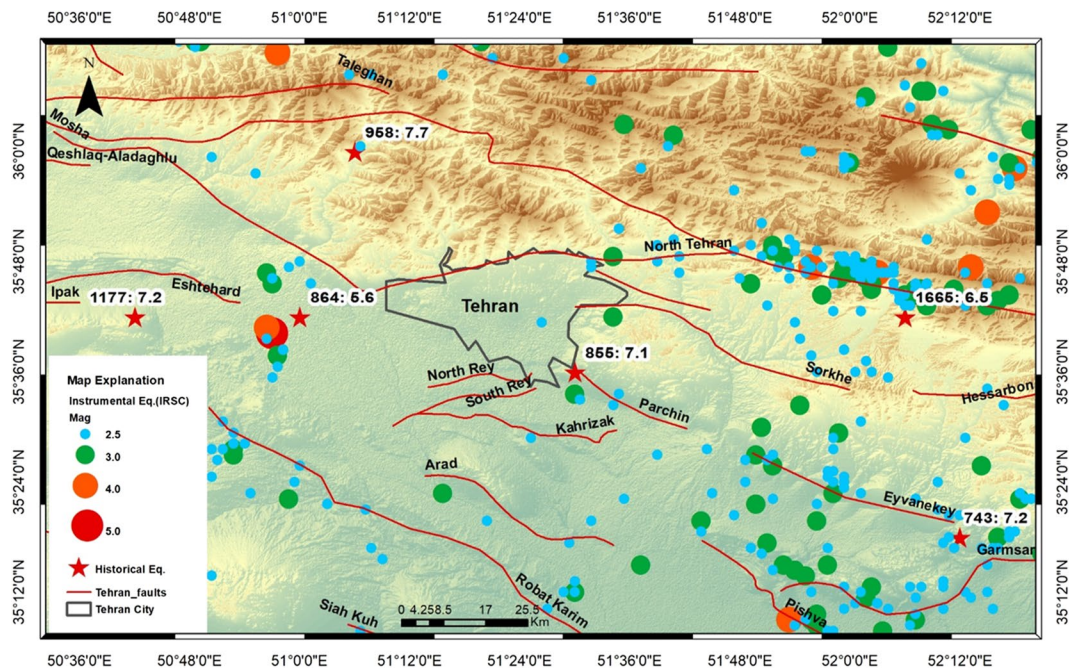


**Fig. 1** Topographic map of the central Alborz Mountains (north of Tehran) and northern Central Iran (south of Tehran). The border of the city, the historical seismicity (red stars), and the instrumental seismicity around Tehran (colored circles) are also shown

life, property destruction, and economic damage is very high (Berberian and Yeats 1999, 2001; JICA 2000; Jackson 2006; Zarrineghbal et al. 2021). Since the strong motion data is sparse in Tehran, simulation methods are the preferred approach for seismic hazard evaluation. In the following sections, we will examine the role of the site effect in the simulation results.

### 3 Strong ground motion records and data processing

The acceleration data was collected by the Iran strong motion network of the Road, Housing, and Urban Development Research Center. This network started its activities since 1973 and at present it consists of 1160 digital strong motion accelerographs. Most of the accelerograph units are concentrated in seismically active or densely populated and industrialized areas. Here, 294 records from 63 stations in and around Tehran city were used to calculate the H/V curve as well as the near-surface high-frequency attenuation parameter ( $\kappa$ ). The majority of the

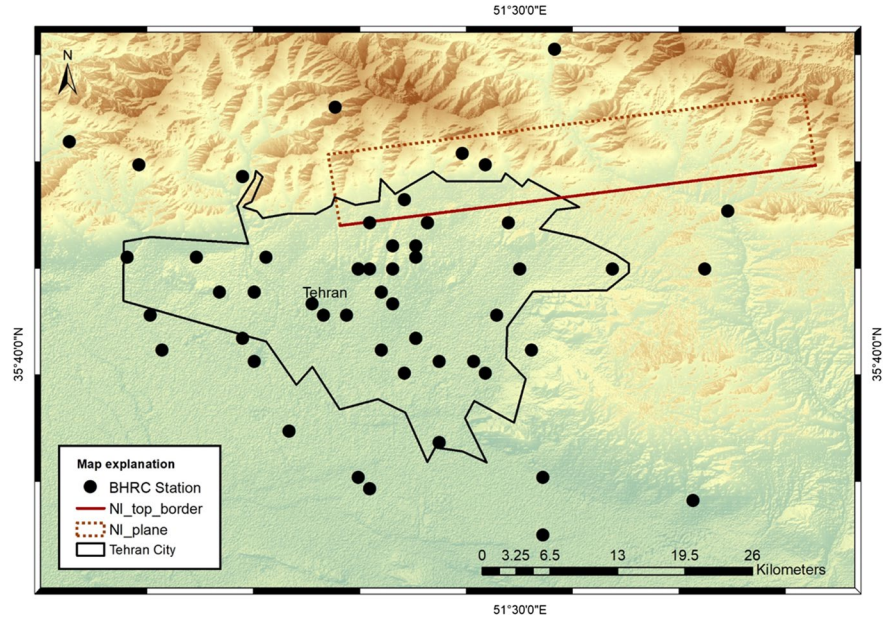
accelerometers are SSA-2, which have a frequency response range of zero to 50 Hz and can be used for a wide range of applications. The sampling frequency of the records is 200 Hz. Figure 2 shows the location of BHRC stations and Fig. 3 shows the studied earthquakes around Tehran and also stations with two records or more. The selected dataset consists of earthquakes in the magnitude range  $M_{2.5}$ –6.5 recorded at distances up to 200 km (Fig. 4).

Regarding the data processing, the steps are as follows: (1) baseline correction, (2) selection of the shear wave window, (3) applying a 5% cosine filter on each end of the signal, (4) using zero-padding to increase the number of signal samples to the next power of 2, (5) calculating the Fourier spectrum of the signal using the FFT algorithm, (6) band-pass filtering based on signal to noise ratio, (7) Fourier spectrum smoothing with the Konno-Ohmachi method ( $be=40$ ). Note that, in step (6) to reduce the dispersion of the results and to improve the accuracy of the analysis results, we eliminate the records with an SNR of less than 5 dB in the 0.05–20 Hz frequency.

To isolate the S-wave window, we used the technique described in Sadeghi-Bagherabadi et al. (2020).



**Fig. 2** Tehran’s borders and locations of the BHRC stations. The thick red line shows Niavaran fault top border



The acceleration envelope is computed using the Hilbert transform of the records’ horizontal components. As seen in Fig. 5, the envelope often grows as the S-wave arrives, and it begins to decay at the end of the direct S-wave window. To eliminate the

coda wave, we selected the end of the S-wave window where the cumulative envelope function starts to decrease.

To determine the horizontal to the vertical ratio (H/V ratio), the signal Fourier amplitude spectrum

**Fig. 3** Distribution of the study earthquakes around Tehran (colored circles) and the BHRC stations with two records or more (colored triangles)

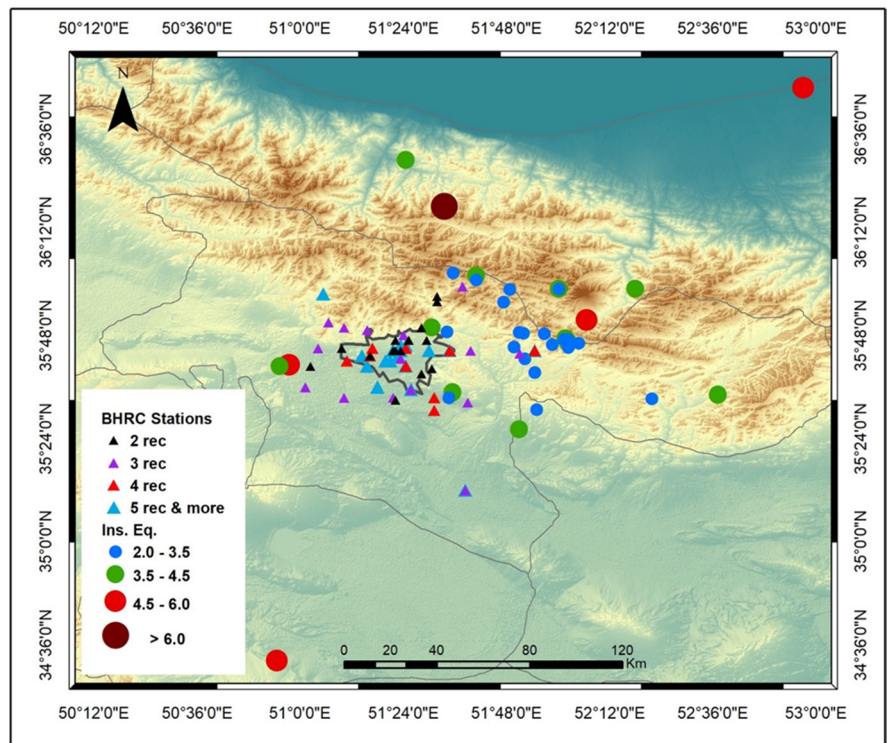
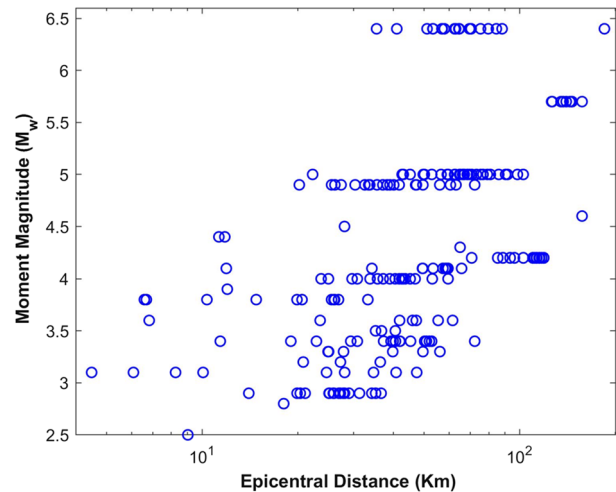


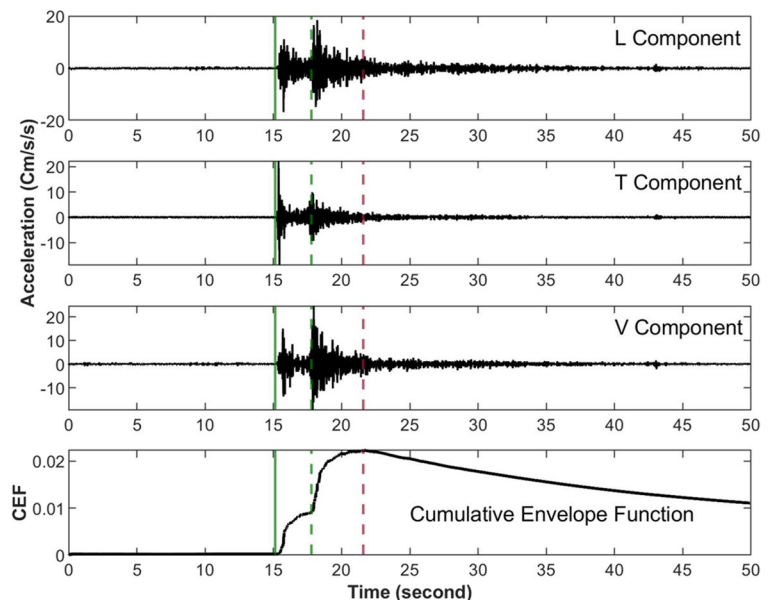
**Fig. 4** Magnitude-distance distribution of records

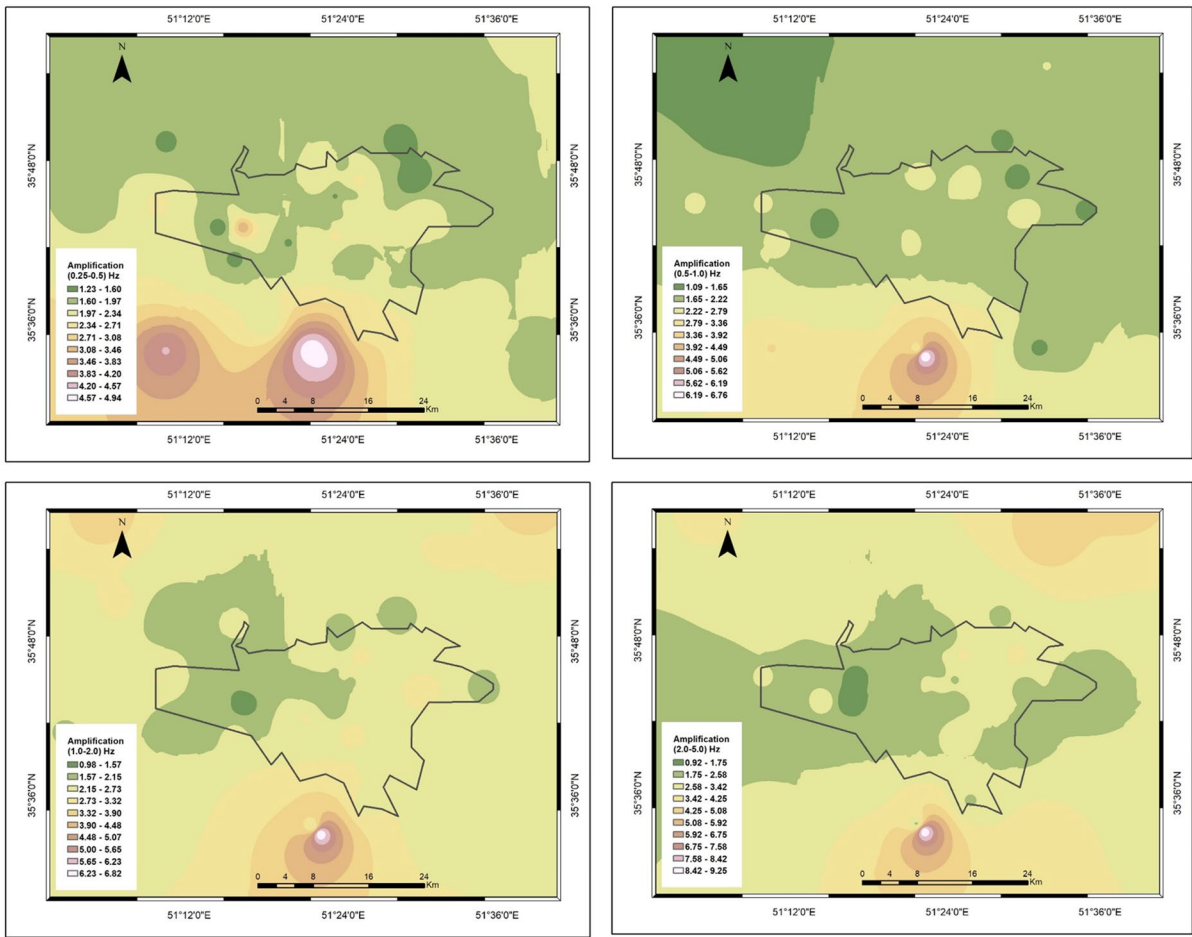


of horizontal components was divided into the corresponding vertical component, and its geometric mean was obtained for each record. Then, the H/V ratio for each station was calculated using the geometric mean, in accordance with the records kept at that station. The results of mean average H/V ratios and standard deviations at different stations are shown in Appendix Figure 18B. It is common to replace the site amplification by the H/V ratio (see Motazedian (2006) for details). So, the meaning of amplification here is the H/V ratio. Figure 6 shows the distribution of the maximum H/V (amplification) at each site and for four frequency ranges.

According to Japan Road Association (1980), the dominant period is less than 0.2 s for rock and stiff soil sites (SC-I), 0.2–0.4 s for hard soil sites (SC-II), 0.4–0.6 s for medium soil sites (SC-III) and greater than or equal to 0.6 s for soft soil sites (SC-IV) (Table 2). On the other hand, Zare et al. 1999, Sinaeian 2006 and Ghasemi et al. 2009, recommended different ranges of fundamental periods at different site classes in Iran (Table 3). The identification method suggested by Zhao et al. (2004), which was based on a quadratic function fit to the H/V spectral ratios at three samples around the peak, was used to ascertain the dominant period. As can be seen in

**Fig. 5** Example accelerom-eter data for three components and the Cumulative Envelope Function (CEF) that was used to choose the direct S-wave window (Kinoshita 1994). P and S. wave arrival timings are indicated by solid and dashed green lines, respectively. The red dashed line indicates where the S-wave window ends





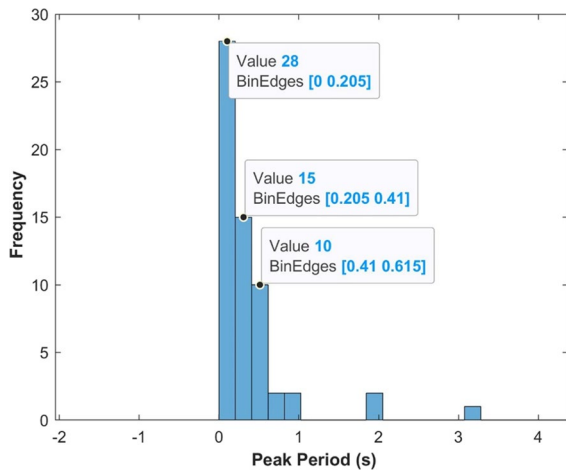
**Fig. 6** Amplification maps (H/V ratio) from BHRC stations showing the level of amplification at Tehran basin at four frequency ranges ([0.1 0.5], [0.5 1.0], [1.0 2.0], [2.0 5.0] Hz)

Fig. 7, the main periods in the various site types are within the limits provided by the Japan Road Association (Japan Road Association 1980). So, the stations were divided into four categories based on the dominant period. Figure 8 shows the average horizontal-to-vertical Fourier amplitude ratio and standard deviation at different periods for each site class.

According to Motazedian (2006), although the amount of amplification of the vertical component of the wave might be insignificant compared to the horizontal component, due to the presence of near-surface attenuation with a different amount of  $\kappa$  in the two components, it is necessary to multiply the factor  $\exp(-\kappa, \pi f)$  in the H /V ratio to

**Table 3** Criteria defined by different studies for site classification in Iran

	Zare et al. 1999	Sinaeian 2006	Ghasemi et al. 2009
Site classes	Fundamental period (s)	Fundamental period (s)	Fundamental period (s)
SC-I	$T \leq 0.06$	$T \leq 0.12$	$T \leq 0.2$
SC-II	$0.06 < T \leq 0.2$	$0.12 < T \leq 0.2$	$0.2 < T \leq 0.25$
SC-III	$0.2 < T \leq 0.5$	$0.2 < T \leq 0.5$	$0.25 < T \leq 0.5$
SC-IV	$T > 0.5$	$T > 0.5$	



**Fig. 7** Histogram of peak period from 294 records from 63 stations

derive an estimate of horizontal site effects. The slope of the smoothed acceleration Fourier spectrum amplitude plot on a logarithmic scale based on frequency on a linear scale at high frequencies, more than 5 Hz, was used in this work to calculate the kappa coefficient for each record (Fig. 9). The slope was determined using the least squares approach. Figures 10 and 11 display the distribution of kappa factors estimated for the horizontal and vertical components of all records against

epicentral distance. As might be predicted, kappa is a distance-dependent characteristic since inelastic attenuation depends on frequency.

The best fits for horizontal and vertical kappa are as follows:

$$\kappa_h(s) = 0.000025(0.000061)r + 0.047(0.0042) \quad (3)$$

$$\kappa_v(s) = 0.000085(0.000056)r + 0.034(0.0038)$$

where values in parentheses are standard errors of coefficients. Site effects amplitudes for the four aforementioned categories are shown in Fig. 12. The components of  $\kappa_0$  and  $\kappa_r$  are listed in Table 4. The vertical  $\kappa_0$  ( $\sim 0.034$ ) is substantially less than the horizontal one ( $\sim 0.047$ ), indicating that the near-site S-wave velocity structure has a far lower impact on the vertical motion. Our findings marginally deviate from the values found in Motazedian (2006), but they are nevertheless consistent. A similar analysis was performed by Motazedian (2006) for the Alborz Mountains of northern Iran, where he determined vertical and horizontal  $\kappa_0$  values of 0.029 and 0.05, respectively. Zafarani et al., (2012) estimated  $\kappa_0$  values of 0.02 and 0.05, for vertical and horizontal components respectively, for the same area. Also, Davatgari Tafreshi et al. (2022) estimated a value of 0.044 for horizontal kappa in Northern Iran.

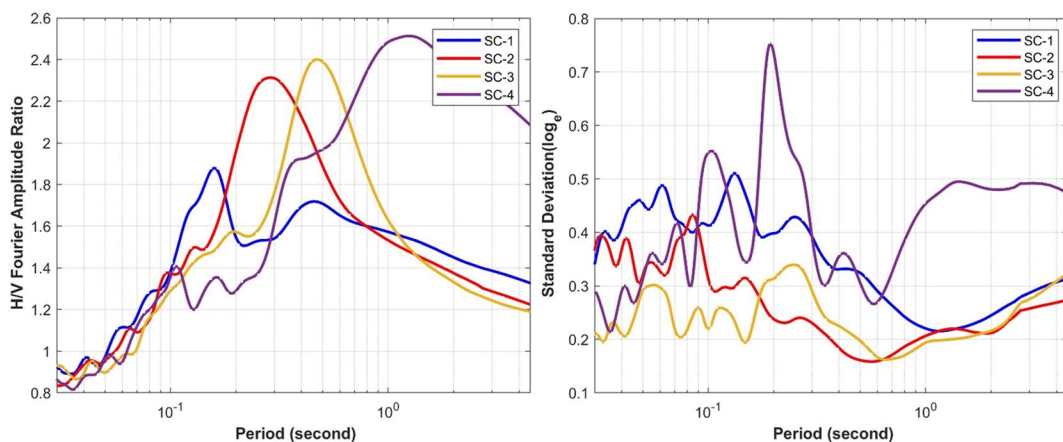


**Fig. 8** (left) Average horizontal to vertical Fourier amplitude ratio (right) and corresponding standard deviations at different periods for each site class



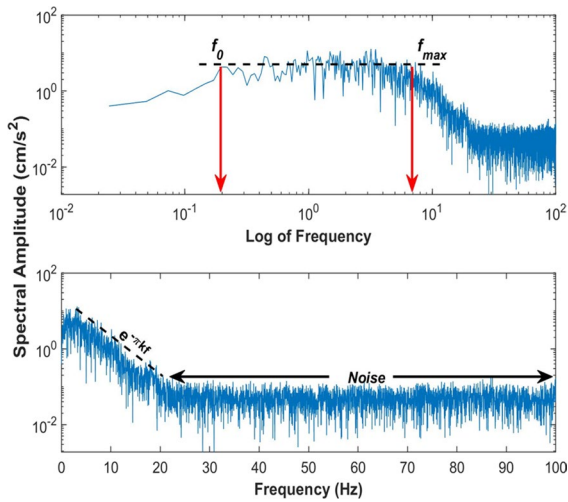


**Fig. 9** Fourier amplitude spectrum of the longitudinal component of strong ground acceleration recorded at Garm-dareh station during the Baladeh earthquake of 28 May 2004 (Mw=6.3). Accelerograph was a digital SSA-2 recorder with a sampling rate of 200/s. (up) Log–log axes. (down) Linear–log axes. Here the kappa is estimated as 0.051 s

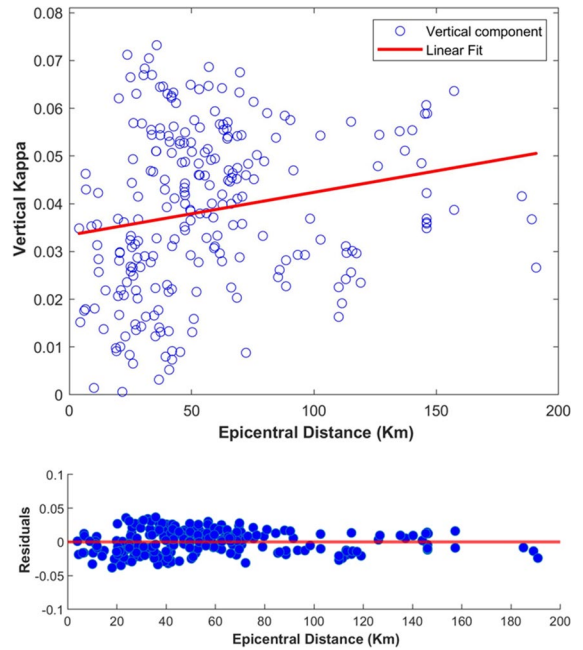


**Fig. 11** Kappa distribution against epicentral distance for vertical component and its residuals

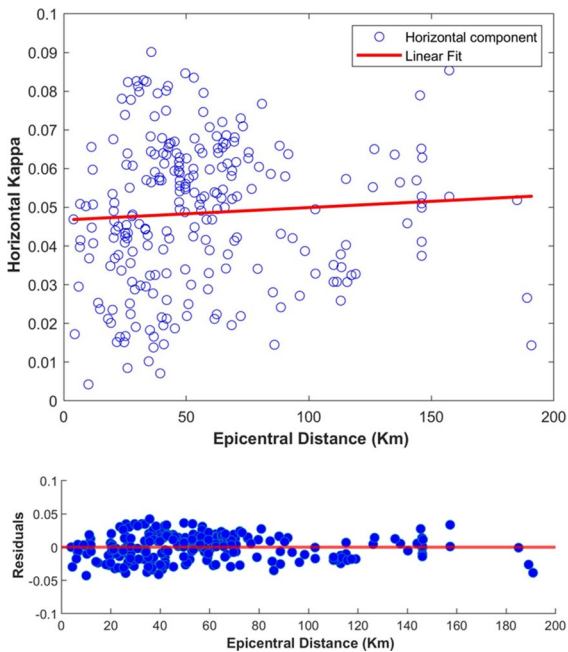


**Fig. 10** Kappa distribution against epicentral distance for horizontal component and its residuals

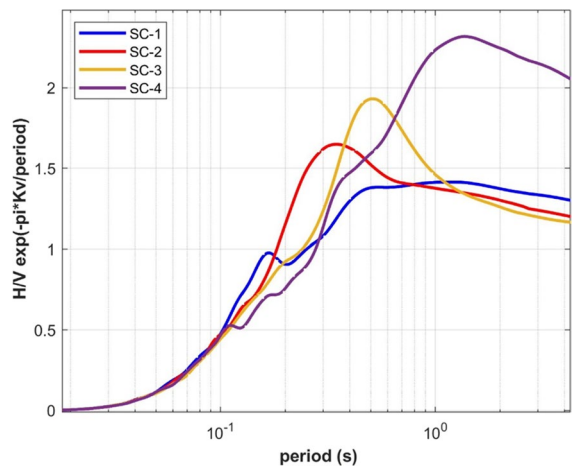


**Fig. 12** Average horizontal to vertical Fourier amplitude ratio with applied near-surface vertical attenuation

**Table 4** Near-surface attenuation parameters  $\kappa_0$  and  $\kappa_R$  estimated from the high-frequency content of horizontal and vertical accelerograms and their comparison with previously published results

$\kappa = \kappa_0 + \kappa_R \mathbf{R}$		Component	Reference	Region
$\kappa_0$	$\kappa_R$			
0.047	0.000025	Horizontal	This study	Tehran
0.034	0.000085	Vertical		
0.044	0.000137		Davatgari Tafreshi et al. 2022	Northern Iran
0.05	0.0001	Horizontal	Zafarani et al. 2012	
0.02	0.0002	Vertical		
0.05	-	Horizontal	Motazedian 2006	
0.029	0.0002	Vertical		

#### 4 Taking site effect into account when simulating an earthquake

The signal amplitude can be amplified or de-amplified by near-surface site effects at different periods, as was previously described. We simulated an earthquake scenario on the Niavaran fault in the north of Tehran here to examine this effect. According to Abbassi and Farbod (2009), the Niavaran fault is a 45-km-long high-angle left-lateral strike-slip fault that dips to the north. The cutting of the Qt1 deposit on the detailed geological map seen on the fault's western terminal is another indicator of its activity. In the present study, numerical simulations of a Mw = 7.0 earthquake rupture of the Niavaran fault are carried out through the finite difference method ( $f < 1.0$  Hz). Then the stochastic finite fault method is used for quantifying ground motion values at higher frequencies (1.0–20.0 Hz). Finally, the broadband simulation results are obtained by the approach of Mai and Beroza (2003).

#### 4.1 Synthesizing seismograms at low frequency ( $f < 1.0$ Hz)

Three-dimensional wave propagation can be used to effectively represent the wave propagation due to the fault rupture process. Here, a horizontally layered crustal model (Table 5, Donner et al. 2013) is assumed and a finite difference (FD) method implemented in the FDSim3D code (Kristek and Moczo 2014) is used (with no advantages relative to some other codes like Axitra) to simulate ground motion at low frequencies. Program FDSim3D is designed for the finite-difference (FD) simulation of seismic wave propagation and earthquake ground motion in 3D local surface heterogeneous viscoelastic structures with a planar-free surface. The computational algorithm is based on the explicit heterogeneous FD scheme solving equations of motion for the heterogeneous viscoelastic medium with material interfaces. The velocity-stress FD scheme is 4<sup>th</sup>-order accurate in space and 2<sup>nd</sup>-order accurate in time. The scheme is constructed on a staggered finite-difference grid.

**Table 5** The adopted velocity-density structure used in our simulation (Donner et al. 2013)

Top of layer (km)	$v_p$ (km/s)	$v_s$ (km/s)	$\frac{v_p}{v_s}$ Ratio	Density ( $\frac{gr}{cm^3}$ )	$Q_p$	$Q_s$
0	4.60	2.69	1.71	2.41	580	300
3	5.40	3.16	1.71	2.58	580	300
8	5.94	3.29	1.81	2.69	580	300
14	6.33	3.49	1.81	2.80	580	300
18	6.53	3.57	1.83	2.86	580	300
48	8.07	4.16	1.94	3.33	973	404
80	8.10	4.18	1.94	3.40	973	404

The rupture velocity on the fault has been assumed equal to 2800 m/s, or about 80% of the  $V_S$  value of the fourth crustal layer, where the hypocenters are likely to be located. The overall model dimensions are 75 km × 94 km × 50 km. The final mesh consists of grids with a size of about 500 m and can propagate waves with frequencies up to 1.25 Hz. To take into account the fault’s finiteness and heterogeneity, the fault is divided into a number of subfaults with uniform slip distribution on them. Also, the isosceles triangle with a base of duration  $T_r$  is used as the slip velocity function. The following empirical relationship has been proposed by Somerville et al. (1999) between the value of  $T_r$  and the seismic moment of the target earthquake,  $M_0$ :

$$T_r = 2.0 \times 10^{-9} \times M_0^{1/3} \tag{4}$$

which yields a rise time of 1.43 s for an M7.0 earthquake.

#### 4.2 Synthesizing seismograms at high-frequency ( $f > 1.0$ Hz)

For synthesizing a high-frequency seismogram, we use the EXSIM program. This program is an open-source stochastic extended finite-source simulation algorithm, written in FORTRAN, that generates time series of ground motion for earthquakes (Motazedian

and Atkinson 2005; Boore 2009; Assatourians and Atkinson 2012). The earthquake’s fault surface is divided up into a grid of subsources by EXSIM so that the ground-motion modeling can take into account the finite-fault effects (such as faulting geometry, distributed rupture, and rupture inhomogeneity). Time series from the sub-sources are modelled using the point-source stochastic model developed by Boore (1983, 2003) and popularized by the Stochastic-Method SIMulation (SMSIM) computer code (Boore 2003, 2005). The stochastic point-source model makes the assumption that the source process is focused at a point and that the acceleration time series that are radiated to a site contain both random and deterministic components of ground motion shaking. The average Fourier spectrum, which is given as a function of distance and magnitude, defines the deterministic aspects. The stochastic aspects are handled by modeling the motions as Gaussian noise with the chosen underlying spectrum. The source term (defined by the Fourier spectrum at the source by seismic moment and stress parameter) is multiplied by the path term (defined by elastic attenuation and geometrical spreading) and the site term (crustal amplification and near-surface attenuation) to produce the underlying deterministic spectrum. In addition, EXSIM makes use of the dynamic corner frequency concept (Motazedian and Atkinson 2005), which describes how a rupture starts out with a high

**Table 6** Summary of important model parameters for the Niavaran fault stochastic seismic scenario

Parameter	Value	Reference
Strike, dip	265°, 70°	Abbassi and Farbod (2009)
Magnitude	7.0 (Mw)	-
Fault plane length and width	45, 20 (Km)	Abbassi and Farbod (2009)
Stress drop ( $\Delta\sigma$ )	50 (bar)	Zafarani et al. 2009
Subfault size	2 × 2 (Km)	-
Shear wave velocity ( $\beta$ )	3.5 (Km/s)	Zafarani et al. 2009
Density ( $\rho$ )	2.8 (kg/m3)	Zafarani et al. 2009
$k_v$	0.034	This study
Quality factor	$Q(f) = 101f^{0.8}$	Zafarani et al. 2012
Geometric spreading	$R^{-1} (R \leq 70)$ $R^{0.2} (75 \leq R \leq 150)$ $R^{-0.1} (R > 150)$	Motazedian 2006
Pulsing area percentage	50%	Motazedian and Atkinson 2005
Rupture velocity	0.8 Shear wave velocity	Motazedian and Atkinson 2005
Window function	Saragoni-Hart	-
Path duration	0.1R	-

corner frequency and gradually decreases as the ruptured area expands. Because of this, the simulation results are relatively insensitive to sub-source size. The sum of the source duration and the path duration determines the duration of motion for each sub-source. The time series from the sub-sources are then added in the time domain with a normalization factor and suitable time delays for rupture front propagation. This would produce a complete seismic signal at a site of interest.

Proper plane modeling, fault dimension, and source parameters are crucial elements in stochastic finite fault simulation. In Table 6, a summary of the significant model parameters is provided. According to previous studies (Abbassi and Farbod 2009; Arian et al. 2012), the fault's strike and dip are 265° and 70°, respectively. The Niavaran Fault lacks large instrumentally recorded earthquakes, which makes it difficult to estimate stress drop accurately. In this investigation, the value of stress drop is taken to be 50 bars. This matches the value suggested by Zafarani et al. (2009). The quality factor used in this study was derived from Zafarani et al., (2012). They proposed the form of  $Q(f) = 101f^{0.8}$  for the earthquakes in the northern part of Iran. Based on data from the Kojour earthquake, Motazedian 2006, developed a trilinear geometric spreading function. Here, the same model is used. The percentage of pulsing area is considered 50%; this means that during the rupture of subfaults, at most 50% of all subfaults are active and the remaining are passive. This parameter is proposed by Motazedian and Atkinson (2005), based on the concept of self-healing pulses given in Heaton (1990). Based on the given parameters, scenario time histories are simulated within a square grid cell with 2 × 2 km sizes for the whole of Tehran.

#### 4.3 Combination of low- and high-frequency components

To obtain a broadband seismogram in the time domain, the low and high frequencies are combined to obtain recordings that cover the full range of frequencies of interest (i.e., 0.1–20 Hz) (e.g., Mai and Beroza 2003). Using the scheme given in Eq. 5, the time traces computed by the two techniques are adapted at intermediate frequencies where their domain of validity overlaps:

$$BB(t) = F^{-1} [w_l LF(f)] + F^{-1} [w_h HF(f)] \quad (5)$$

where  $BB$  is the broadband signal in the time domain and  $LF$  and  $HF$  are the low- and high-frequency spectra, respectively.  $F^{-1}$  indicates the inverse Fourier transform, and  $w_l$  and  $w_h$  are smoothed frequency-dependent weighting functions. Both signals are weighted in the transition band so that, at each frequency, the weighting functions are summed to be equal to unity. Using 1 Hz as a transition between high- and low-frequency components is well established (see, e.g., Bielak et al. 2010; Ameri et al. 2012; Olsen et al. 2006.). This is generally attributed to the maximum resolved frequency of coherent motions around this value. This constraint is due to the low resolution of velocity and crustal models.

#### 4.4 Simulation result

Figures 13, 14, 15, and 16 show PSA maps from broadband simulation of scenario earthquakes on the Niavaran fault for different site classes at different periods:  $T = 0.2, 0.5, 1.0,$  and  $4.0$  s, respectively. Also, the maximum values of PSA are shown in Table 7. As can be seen in this table, different site classes cause between 11 and 28% variability in response spectra. Figure 17 shows the comparison of acceleration response spectra at four near-field sample receivers based on assumed model parameters of the Niavaran fault seismic scenario and one of the NGA-West2 ground motion prediction equation (Boore et al. 2014, BSSA) for different site classes. This ground-motion prediction equation (GMPE) provides the computation of median peak ground motions and response spectra for shallow crustal earthquakes in active tectonic regions. Note that the  $V_{S30}$  values for each site class are chosen by Shafiee and Azadi (2007).

## 5 Discussion and conclusions

Recent earthquake damage distributions have demonstrated that the influence of local geology on ground shaking is a significant factor in engineering seismology. Surface geology and  $V_{S30}$  are the two site characterization parameters that have been suggested by the Iranian seismic code (i.e., Standard No. 2800) for site classification. The Japan Road Association (1980)



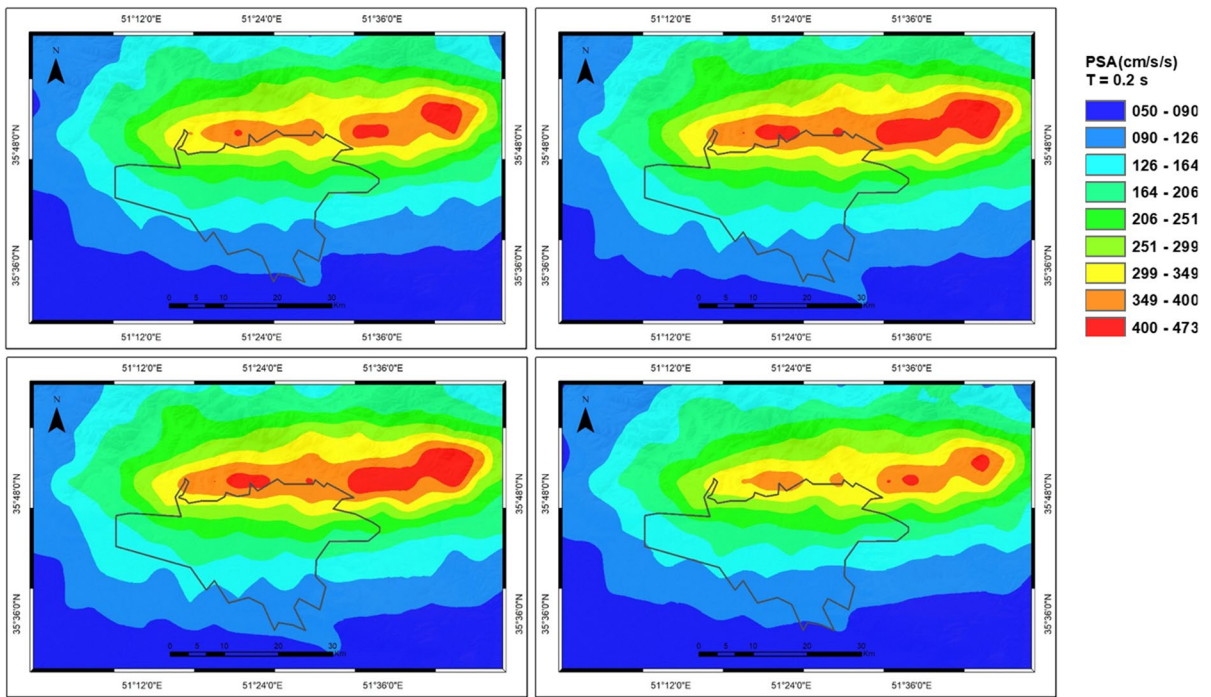


**Fig. 13** Distribution of PSA ( $T=0.2$  s) based on assumed model parameters of the Niavaran fault seismic scenario for different site classes

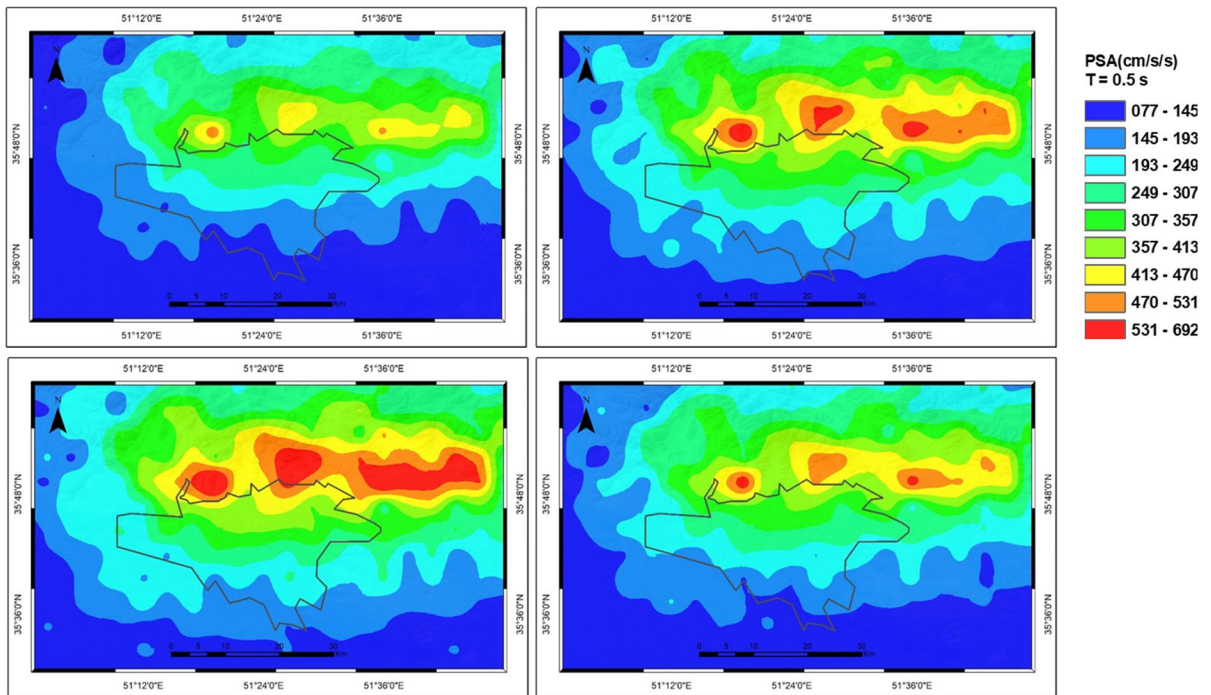


**Fig. 14** Distribution of PSA ( $T=0.5$  s) based on assumed model parameters of the Niavaran fault seismic scenario for different site classes

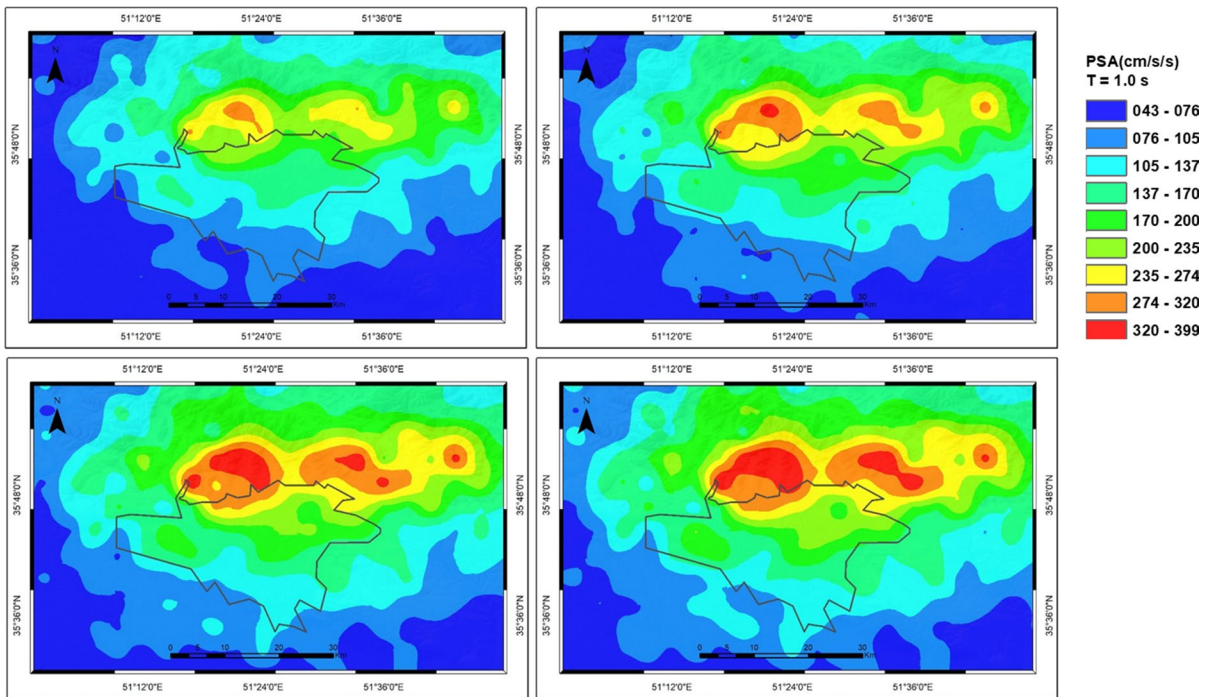


**Fig. 15** Distribution of PSA ( $T = 1.0$  s) based on assumed model parameters of the Niavaran fault seismic scenario for different site classes

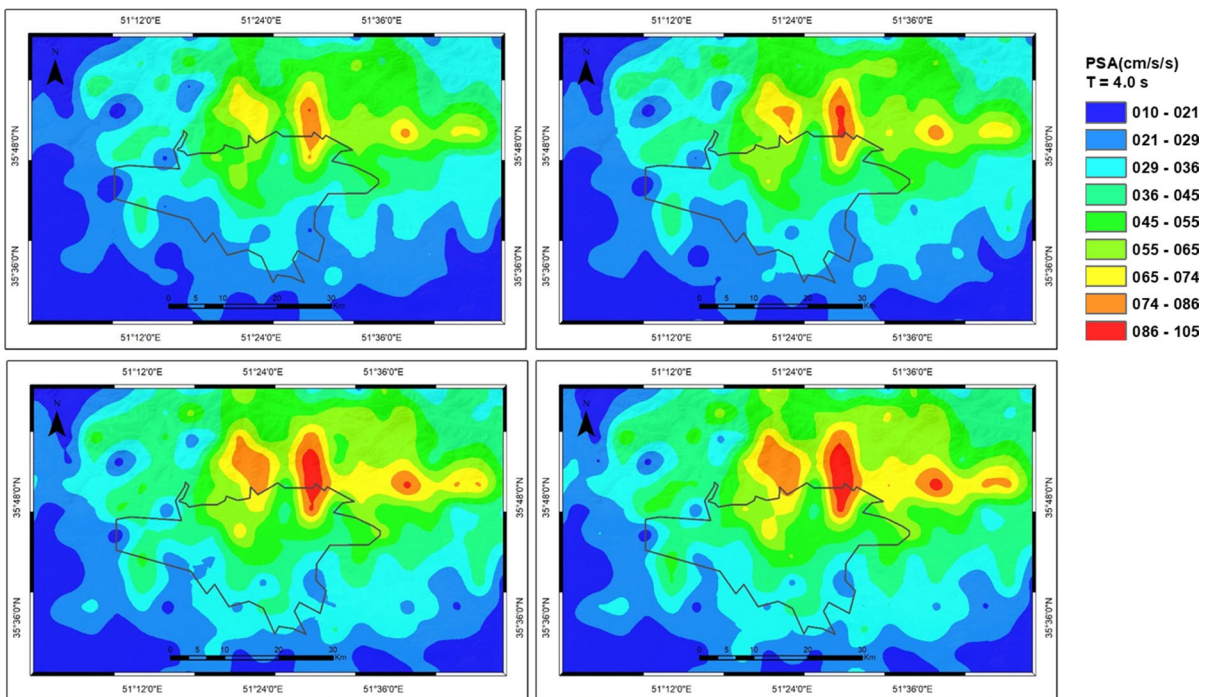


**Fig. 16** Distribution of PSA ( $T = 4.0$  s) based on assumed model parameters of the Niavaran fault seismic scenario for different site classes

**Table 7** Maximum values of PSA at different periods: T=0.2, 0.5, 1.0, and 4.0 s

Period (sec)	PSA (cm <sup>2</sup> )				Change (%)
	Class 1	Class 2	Class 3	Class 4	
0.2	443	470	473	425	11
0.5	552	639	692	595	25
1.0	310	347	392	399	28
4.0	087	093	099	105	20

offered the site parameter of the natural period of the site as an alternative parameter, which was examined in this study using strong motion data in the Tehran

basin. In the Tehran region, it seems a site classification based on a mix of  $V_{S30}$  and the depth of the soil layers rather than precisely following the  $V_{S30}$  method is a more efficient tool for taking into account the deep basin effects. In this way, deep geological profiles and high shear wave velocities are mapped to the resonance frequency, which is one benefit of this classification.

Another goal of this study is to show the spatial distribution of the maximum site amplification for different spectral ordinates and its impact on simulation results. To replace the site amplification with H/V, we need to calculate the kappa factor (for both horizontal and vertical components) in order to remove considerable near-surface

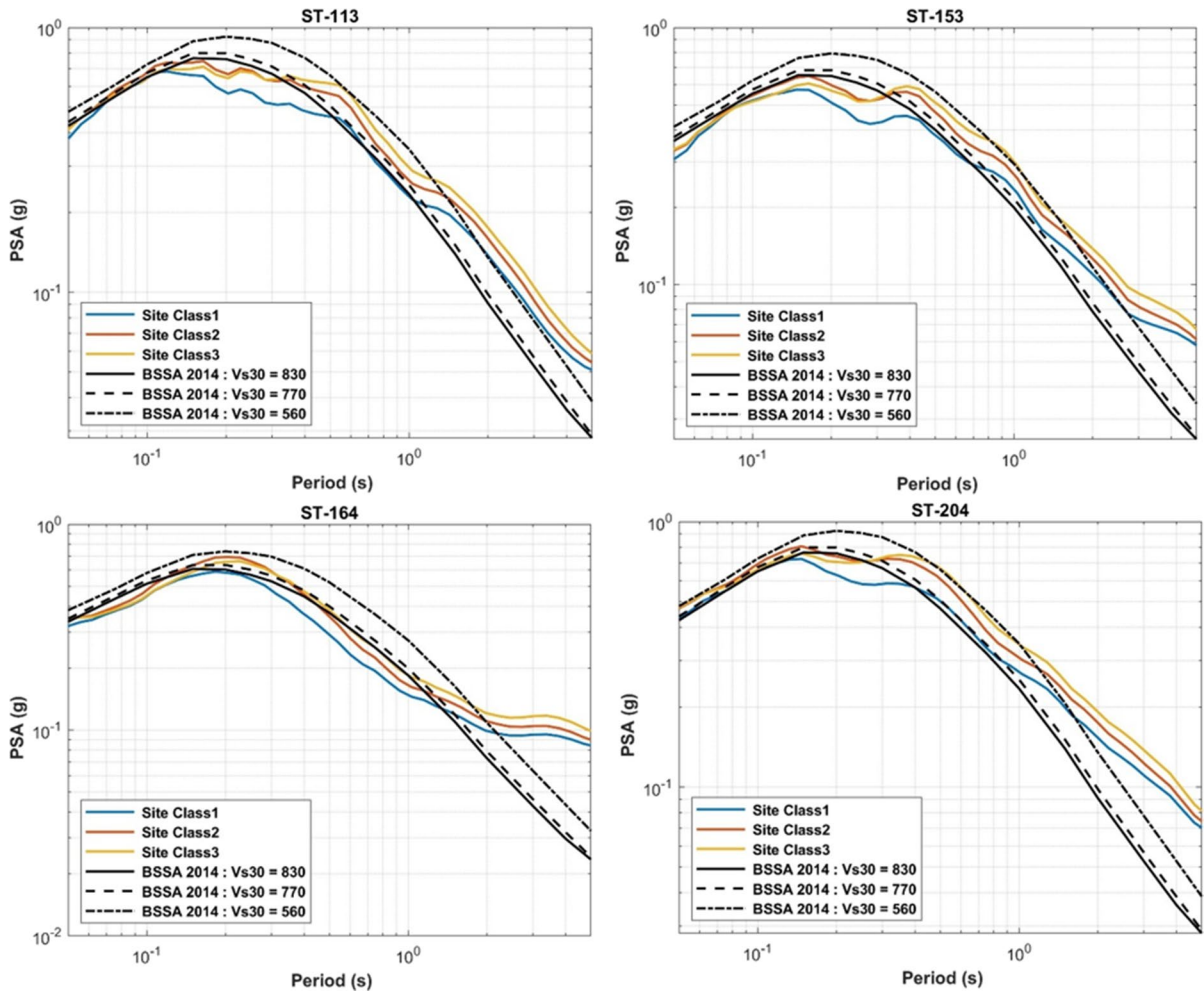


**Fig. 17** Comparison of acceleration response spectra at four near-field sample receivers based on assumed model parameters of the Niavaran fault seismic scenario and Boore et al.

(2014) GMPE for different site classes. The  $V_{S30}$  values for each site class are chosen from Shafiee and Azadi (2007)



high-frequency attenuation of vertical components (Motazedian 2006). So, 294 processed accelerograms obtained from the 63 BHRC stations are used to estimate the corresponding site effects at the recording stations. The H/V ratio was obtained by calculating the signal Fourier amplitude spectrum and the kappa factors for the horizontal and vertical components from the slope of the high-frequency part of the smoothed Fourier acceleration amplitude spectrum. The value of  $\kappa_0$  for horizontal and vertical components are 0.047 s and 0.034 s, respectively.

The findings demonstrate that the mean H/V curves for various site classes considerably differ from one another and take the form of the associated mean H/V ratios. The resulting H/V peak periods for various site types in the Tehran region are within the limits provided by the Japan Road Association (Japan Road Association 1980).

Considering the fact that there is little information on the deep basin layers in Tehran, this strategy is excellent for classifying seismic site effects. However, the site categorization results are still in the early stages and additional research utilizing

more geological and geotechnical data is required (e.g., surface geology, crosshole, and downhole shear wave velocities).

Moreover, because the outcomes of such approaches are closely tied to the number of strong motions recorded in the desired location, the method used in this paper should be utilized with caution. Moreover, taking to account the fact that the database is dominated by small to moderate events and most stations are located at a distance more than 20 km from the epicenter (see Fig. 4), we expect a low level of soil-nonlinearity effects (see also Mousavi et al. 2007).

For the purpose of exploring site effect consideration, we use the hybrid method composed of the finite difference method for low frequencies (< 1 Hz) and a stochastic finite fault method for high-frequency radiation (> 1 Hz) to simulate an earthquake scenario on the Niavaran fault, which is located in the north of Tehran. As a result, different site classes cause between 11 and 28% variability in response spectral amplitudes at different periods ( $T = 0.2, 0.5, 1.0, \text{ and } 4.0 \text{ s}$ ).



**Table 8** BHRC stations used in the study

Station number	Station name	Latitude (deg)	Longitude (deg)	T-Angle (deg)	L-Angle (deg)	Number of Records	Vs30
1	BUMI	35.73	51.85	90	0	3	
2	CGG	35.54	51.65	100	10	3	
3	FSH	35.95	51.53	90	0	2	
4	FSH2	35.93	51.53	90	0	2	
5	GAR	35.75	51.07	290	200	3	
6	GHN	35.56	51.52	90	0	4	
7	GLN	35.51	51.52	210	120	4	
8	GMD	35.99	51.63	185	95	3	
9	KJR2	35.96	51.09	300	210	6	
10	KOD	35.85	51.11	290	200	3	
11	LAV	35.20	51.64	90	0	3	
12	LAV1	35.20	51.64	90	0	23	
13	NAS1	35.56	51.17	90	0	3	
14	RDH	35.74	51.91	270	180	4	
15	RDH1	35.74	51.91	90	0	6	
16	SHY1	35.68	51.04	90	0	2	
17	SLQ1	35.82	51.26	90	0	3	
18	TEH01	35.59	51.43	90	0	3	
19	TEH17	35.67	51.51	90	0	2	693
20	TEH18	35.74	51.37	90	0	2	
21	TEH22	35.74	51.39	165	75	2	
22	TEH29	35.68	51.41	90	0	4	
23	TEH30	35.83	51.47	220	130	2	481
24	TEH52	35.74	51.58	90	0	4	593
25	TEH59	35.78	51.42	290	200	2	
26	TEH60	35.78	51.42	100	10	2	
27	TEH61	35.78	51.42	100	10	2	
28	TEH62	35.78	51.42	100	10	2	
29	TEH63	35.78	51.42	100	10	2	
30	TEH67	35.72	51.27	90	0	4	613
31	TEH68	35.72	51.27	90	0	2	613
32	TEH70	35.74	51.58	90	0	13	

Table 8 (continued)

Station number	Station name	Latitude (deg)	Longitude (deg)	T-Angle (deg)	L-Angle (deg)	Number of Records	Vs30
33	TEH75	35.55	51.37	90	0	2	
34	TEH90	35.74	51.36	90	0	5	
35	TEH91	35.74	51.36	90	0	9	
36	TH001	35.74	51.36	90	0	12	
37	TH004	35.74	51.39	90	0	7	
38	TH005	35.70	51.33	90	0	7	
39	TH006	35.74	51.50	90	0	8	
40	TH007	35.76	51.39	90	0	8	
41	TH009	35.70	51.35	90	0	7	
42	TH010	35.59	51.43	90	0	5	
43	TH012	35.68	51.41	90	0	6	
44	TH013	35.76	51.41	90	0	6	
45	TH014	35.72	51.38	90	0	7	
46	TH015	35.60	51.30	90	0	6	
47	TH016	35.75	51.28	90	0	4	
48	TH017	35.72	51.24	90	0	7	
49	TH019	35.68	51.26	90	0	6	
50	TH021	35.70	51.18	90	0	4	
51	TH022	35.68	51.41	90	0	6	
52	TH028	35.78	51.37	90	0	2	
53	TH300	35.74	51.36	90	0	2	
54	TH302	35.74	51.66	90	0	3	
55	TH303	35.78	51.49	90	0	2	
56	TH304	35.56	51.36	90	0	3	
57	TH305	35.65	51.47	90	0	2	
58	TH306	35.71	51.39	90	0	3	
59	TH307	35.80	51.40	90	0	3	
60	TH309	35.75	51.16	90	0	2	522
61	TH310	35.75	51.41	90	0	4	
62	VAH1	35.60	51.02	90	0	3	300
63	VAR	35.83	51.17	5	275	3	

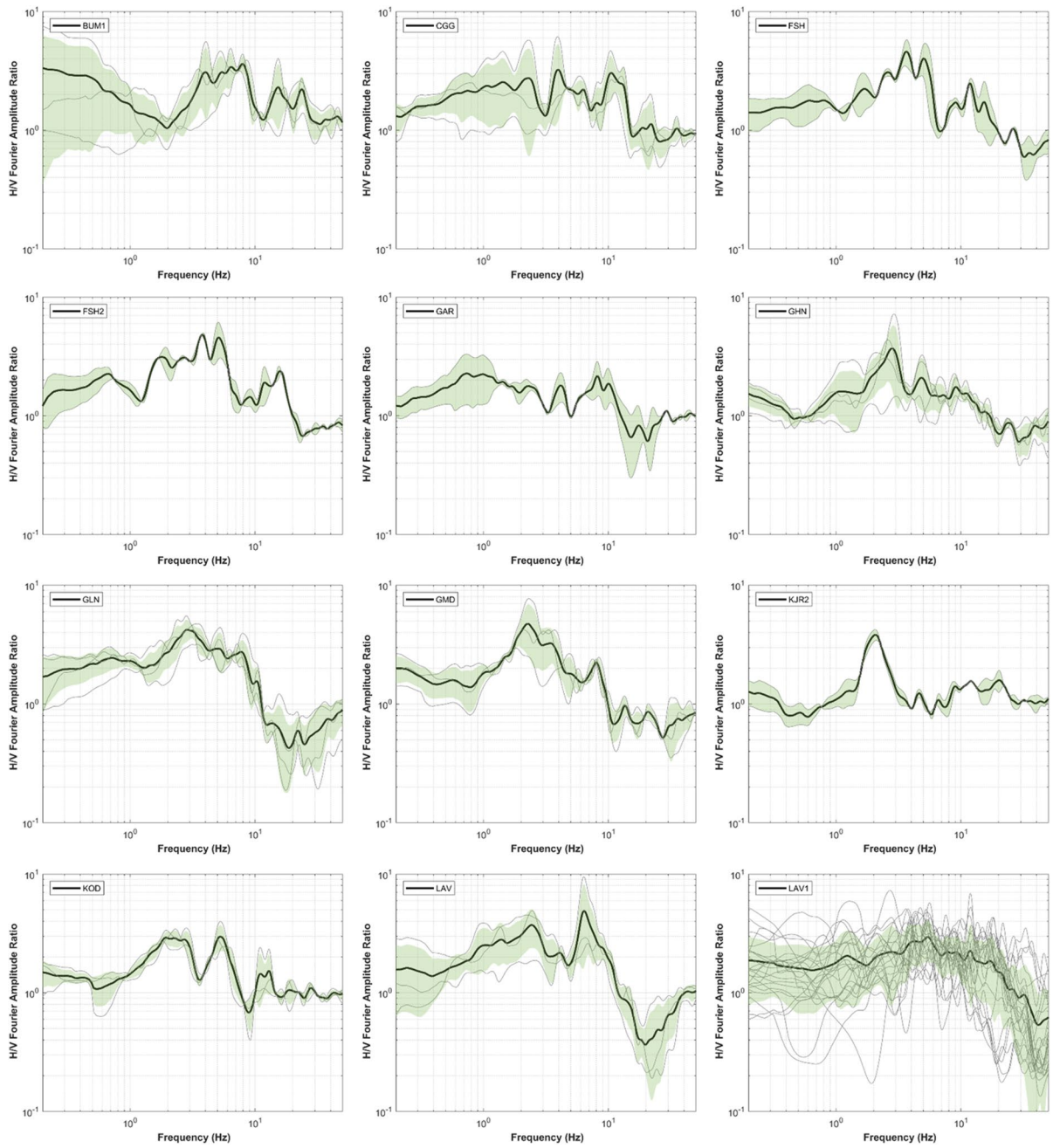


**Fig. 18** Mean average H/V ratios (black curves) and standard deviations (green area) at 63 stations

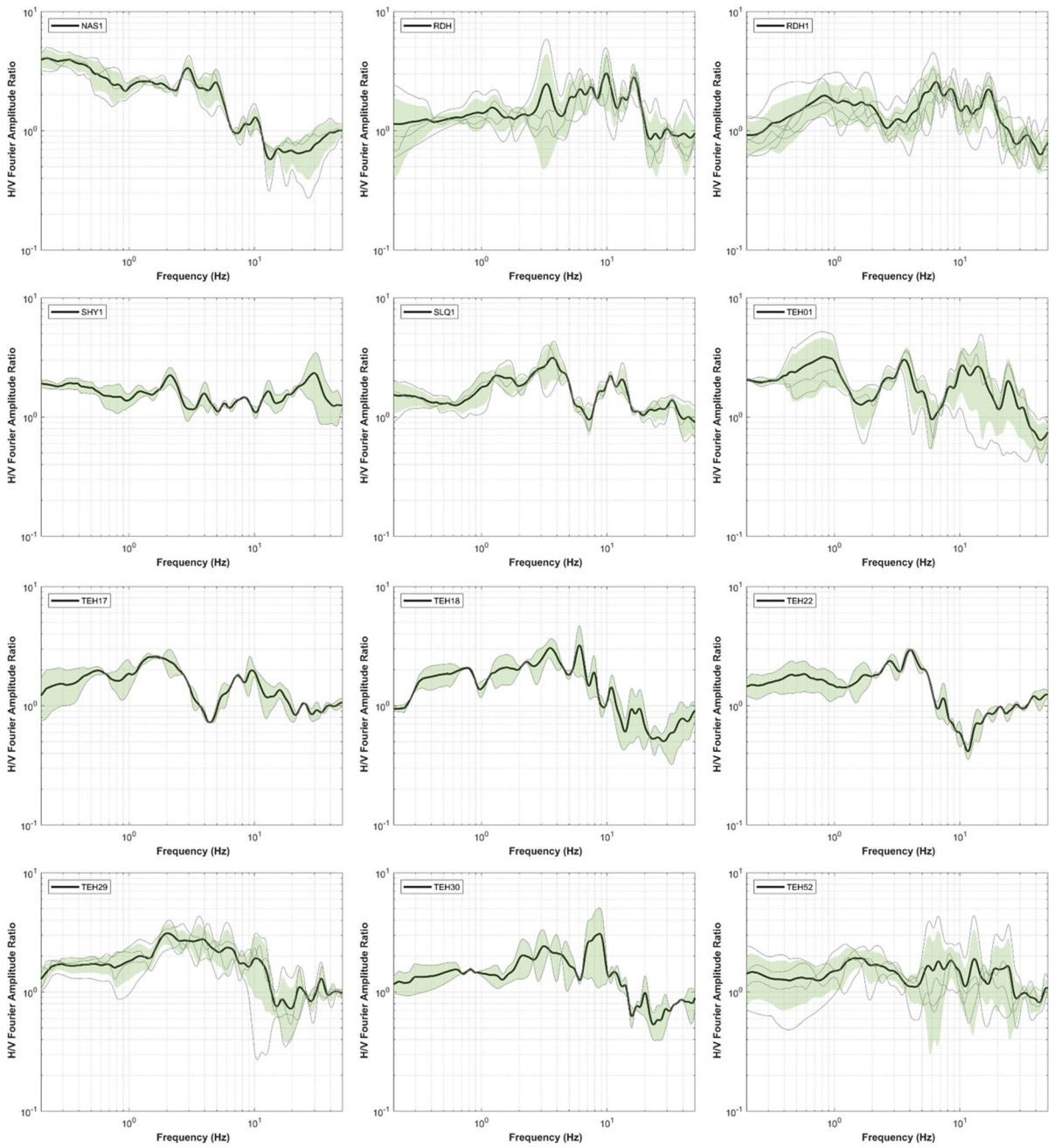


Fig. 18 (continued)



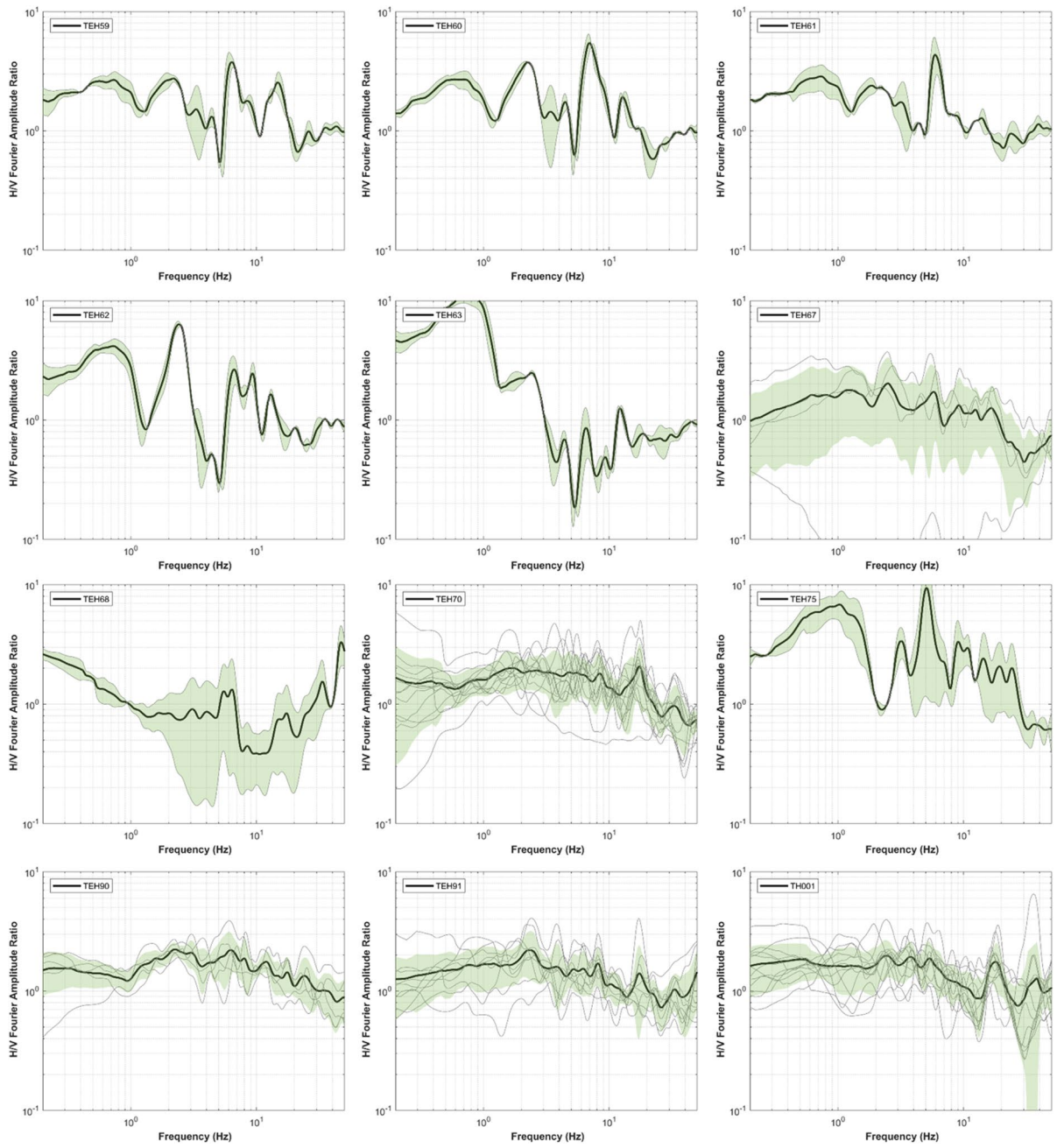


Fig. 18 (continued)

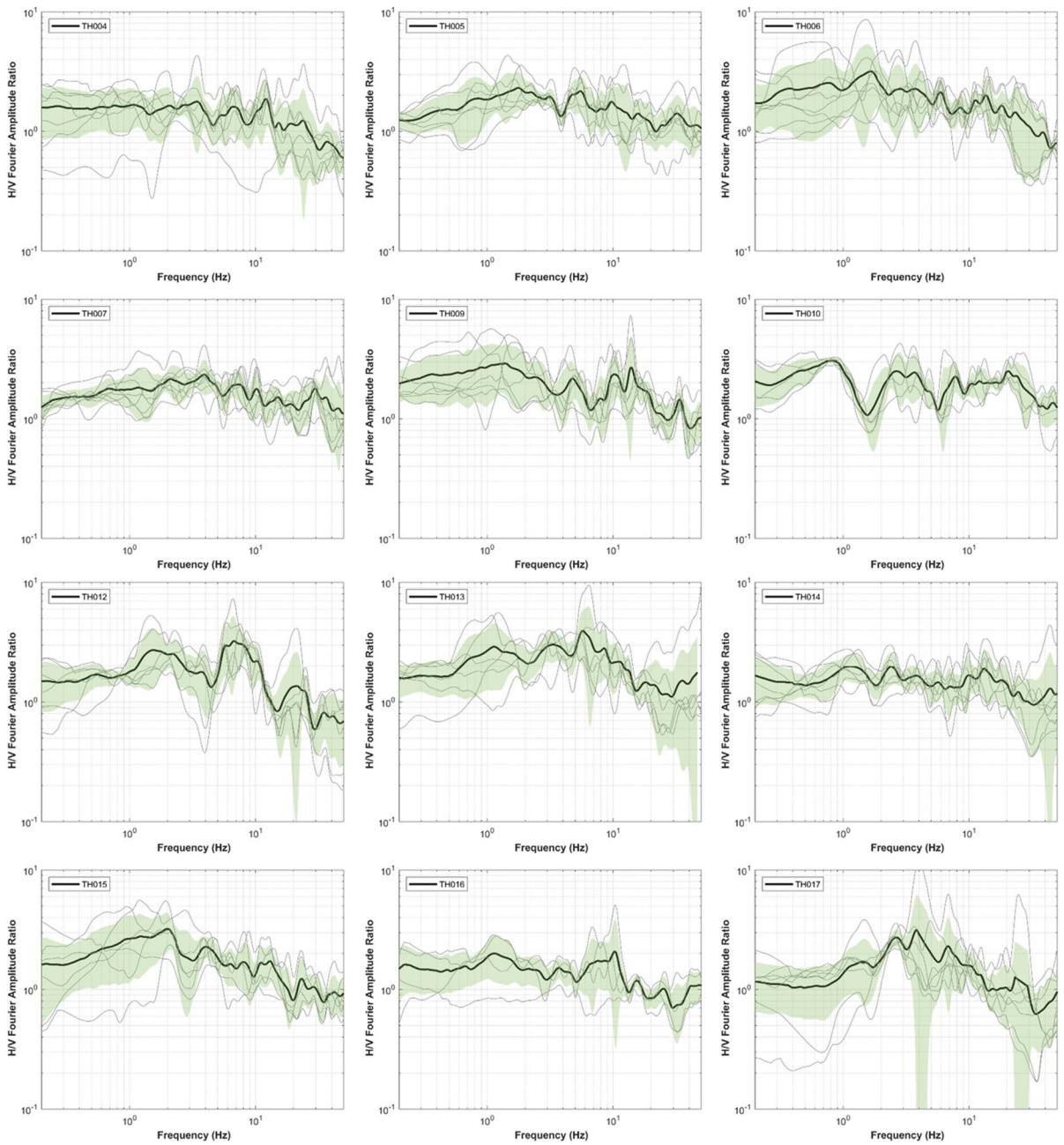


Fig. 18 (continued)



Fig. 18 (continued)



**Acknowledgements** This work was supported by the International Institute of Earthquake Engineering and Seismology. We would like to acknowledge Building and Housing Research Center that provided strong motion data. This study was supported by the International Institute of Earthquake Engineering and Seismology (IIEES), and is a part of the project: “Physics Based Probabilistic Seismic Hazard Analysis by considering uncertainties, case study: Tehran region.”

**Author contribution** **Reza Alikhanzadeh:** Material preparation, data collection, and analysis, simulation, writing the manuscript.

**Hamid Zafarani:** Discussed the results and commented on the manuscript and supervision.

**Behzad Hassani:** Discussed the results and commented on the manuscript.

**Data availability** The data generated during the current study are available from the corresponding author upon reasonable request.

#### Declarations

**Ethics approval and consent to participate** Not applicable.

**Consent for publication** Not applicable.

**Competing interests** The authors declare no competing interests.

#### Appendix

Table 8 and Figure 18

#### References

- Abbassi MR, Farbod Y (2009) Faulting and folding in quaternary deposits of Tehran’s piedmont (Iran). *J Asian Earth Sci* 34:522–531
- Ameri G, Gallovic F, Pacor F (2012) Complexity of the Mw 6.3 2009 L’Aquila (central Italy) earthquake: 2. Broadband strong motion modeling. *J Geophys Res Solid Earth* 117:B04308
- Anderson J, Hough S (1984) A model for the shape of the Fourier amplitude spectrum of acceleration at high frequencies. *Bull Seism Soc Am* 74:1969–1993
- Arian M, Bagha N, Khavari R, Noroozpoor H (2012) Seismic sources and neo-tectonics of Tehran area (North Iran). *Indian J Sci Technol* 5(3):2379–2383
- Assatourians K, Atkinson G (2012) EXSIM12: A Stochastic Finite-Fault Computer Program in FORTRAN, <http://www.seisimotoolbox.ca>. Accessed Nov 2014
- Bard PY, Bora SS, Hollender F, Laurendeau A, Traversa P (2019) Are the Standard VS-Kappa host-to-target adjustments the only way to get consistent hard-rock ground motion prediction? *Pure Appl Geophys* 177(5):2049–2068
- Berberian M (1976) Contribution to the Seismotectonics of Iran, Part II. *Geol Surv Iran* 39, 518p (in English) with five color maps
- Berberian M, Yeats RS (1999) Patterns of historical earthquake rupture in the Iranian Plateau. *Bull Seismol Soc Am* 89(1):120–139. <https://doi.org/10.1785/BSSA0890010120>
- Berberian M, Yeats RS (2001) Contribution of archaeological data to studies of earthquake history in the Iranian plateau. *J Struct Geol* 23:563–584
- Beresnev I, Atkinson GM (1997) Shear wave velocity survey of seismographic sites in eastern Canada: calibration of empirical regression method of estimating site response. *Seism Re S Lett* 68:981–987
- Bielak et al (2010) The ShakeOut earthquake scenario: Verification of three simulation sets. *Geophys J Int* 180:375–404. <https://doi.org/10.1111/j.1365-246X.2009.04417.x>
- Bonnefoy-Claudet S, Cotton F, Bard P-Y (2006) The nature of noise wavefield and its applications for site effects studies. *Earth-Science Reviews*. <https://doi.org/10.1016/j.earscirev.2006.07.004>
- Boore DM (1983) Stochastic simulation of high-frequency ground motions based on seismological models of the radiated spectra. *Bull Seismol Soc Am* 73:1865–1894
- Boore DM (2003) Simulation of ground motion using the stochastic method. *Pageoph* 160(3):635–676. <https://doi.org/10.1007/PL00012553>
- Boore DM (2009) Comparing stochastic point-source and finite-source ground-motion simulations: SMSIM and EXSIM. *Bull Seismol Soc Am* 99:3202–3216. <https://doi.org/10.1785/0120090056>
- Boore DM (2005) SMSIM - Fortran programs for simulating ground motions from earthquakes: version 2.3 - a revision of OFR 96-80-A. U.S. Geological Survey Open-File Report 00-509
- Boore D, Stewart J, Seyhan E, Atkinson G (2014) NGA-West2 Equations for Predicting PGA, PGV, and 5% Damped PSA for Shallow Crustal Earthquakes. 30:1057–1085. <https://doi.org/10.1193/070113EQS184>
- Building and Housing Research Center (2014) Iranian code of practice for seismic resistant design of buildings, Standard No. 2800, 4th edn. Tehran, Iran
- Davatgari Tafreshi M, Singh Bora S, Ghofrani H, Mirzaei N, Kazemian J (2022) Region- and site-specific measurements of kappa and associated variabilities for Iran. *Bull Seismol Soc Am* 112(6):3046–3062
- Donner S, Roessler D, Krueger F, Ghods A, Strecker M (2013) Segmented seismicity of the M w 6.2 Baladeh earthquake sequence (Alborz Mountains, Iran) revealed from regional moment tensors. *Journal of Seismology*. 17. <https://doi.org/10.1007/s10950-013-9362-7>
- BSSC (2000) NEHRP Recommended Provisions for New Building and Other Structures, Part 1: Provisions (FEMA 368). BUILDING SEISMIC SAFETY COUNCIL. Washington, DC
- Fukushima Y, Bonilla LF, Scotti O, Douglas J (2007) Site classification using horizontal to vertical response spectral ratios and its impact when deriving empirical ground-motion prediction equations. *J Earthquake Eng Taylor & Francis* 11(5):712–724
- Ghasemi H, Zare M, Fukushim Y, Sinaeian F (2009) Applying empirical methods in site classification, using response spectral ratio (H/V): a case study on Iranian strong motion network (ISMN). *Soil Dyn Earthq Eng* 29:121–132



- Heaton TH (1990) Evidence for and implications of self-healing pulses of slip in earthquake rupture, *Physics of the Earth and Planetary Interiors*, 64(1). ISSN 1–20:0031–9201
- Jackson J (2006) Fatal attraction: living with earthquakes, the growth of villages into megacities, and earthquake vulnerability in the modern world *Phil. Trans R Soc A*. 3641911–1925. <https://doi.org/10.1098/rsta.2006.1805>
- Japan Road Association. “Specifications for Highway Bridges Part V, Seismic Design”, Maruzen Co., LTD, 1980
- Japan International Cooperation Agency (JICA) (2000). “Centre for Earthquake and Environmental Studies of Tehran (CEST), Tehran Municipality: The Study on Seismic Microzoning of the Greater Tehran Area in the Islamic Republic of Iran”
- Kanai K, Tanaka T (1961) On Microtremors VIII. *Bullet Earthquakes Res Inst* 39:97–114
- Kinoshita S (1994) Frequency-dependent attenuation of shear wave in the crust of the southern Kanto area. *Bull Seismol Soc Am* 59:1387–96
- Kristek, J., Moczo, P., 2014. FDSim3D - The Fortran95 code for numerical simulation of seismic wave propagation in 3D heterogeneous viscoelastic media. [www.cambridge.org/moczo](http://www.cambridge.org/moczo)
- Lee VW, Trifunac MD, Todorovska M, Novikova EI (1995) Empirical equations describing attenuation of peaks of strong ground motion, in terms of magnitude, distance, path effects and site conditions. University of Southern California (Report no. CE 95–02)
- Lermo J, Chavez-Garcia FJ (1993) Site effect evaluation using spectral ratios with only one station. *Bull Seismol Soc Am* 83:1574–1594
- Lussou PPY, Bard F, Cotton Y, Fukushima (2001) Seismic design regulation codes: Contribution of K-net data to site effect evaluation. *J Earthq Eng* 5:13–33
- Mai PM, Beroza G (2003) A hybrid method for calculating near-source, broadband seismograms: application to strong motion prediction. *Phys Earth Planet Int* 137:183–199
- Motaghi Kh, Ghods A (2012) Attenuation of Ground-Motion Spectral Amplitudes and Its Variations across the Central Alborz Mountains. *Bull Seismol Soc Am* 102(4):1417–1428. <https://doi.org/10.1785/0120100325>
- Motazedian D (2006) Region-specific key seismic parameters for earthquakes in northern Iran. *Bull Seismol Soc Am* 96(4A):1383–1395
- Motazedian D, Atkinson GM (2005) Stochastic finite-fault modeling based on a dynamic corner frequency. *Bull Seismol Soc Am* 95:995–1010
- Mousavi M, Zafarani H, Noorzad A, Ansari A, Bargi K (2007) Analysis of Iranian strong-motion data using the specific barrier model. *J Geophys Eng* 4(4):415–428
- Olsen K, Archuleta R (1996) Three-dimensional simulation of earthquakes on the Los Angeles fault system. *Bull Seism Soc Am* 86:575–596
- Olsen K, Akinci A, Rovelli A, Marra F, Malagnini L (2006) 3D ground-motion estimation in Rome, Italy. *Bull Seismol Soc Am* 96:133–146
- Pitarka A, Takenaka H, Suetsugu D (1994) Modeling strong motion in the Ashigara Valley for the 1990 Odawara, Japan, earthquake. *Bull Seism Soc Am* 84:1327–1335
- Rodriguez-Marek A, Rathje EM, Bommer JJ, Scherbaum F, Stafford PJ (2014) Application of single-station sigma and site-response characterization in a probabilistic seismic-hazard analysis for a new nuclear site. *Bull Seism Soc Am* 104(4):1601–1619
- Sadeghi-Bagherabadi A, Sobouti F, Pachhai S, Aoudia A (2020) Estimation of geometrical spreading, quality factor and kappa in the Zagros region, *Soil Dynamics and Earthquake Engineering*, Volume 133. ISSN 106110:0267–7261
- Safak E (2001) Local site effects and dynamic soil behavior. *Soil Dyn Earthq Eng* 21:453–458
- Shafiee A, Azadi A (2007) Shear-wave velocity characteristics of geological units throughout Tehran city, Iran. *J Asian Earth Sci* 29:105–115
- Sinaeian, F (2006) Study on Iran strong motion records, PhD dissertation, International Institute of Earthquake Engineering and Seismology, Tehran, Iran
- Somerville P, Irikura K, Graves R, Sawada S, Wald D, Abrahamson N (1999) Characterizing earthquake slip models for the prediction of strong ground motion. *Seismol Res Lett* 70:59–80
- Yamazaki F, Ansary MA (1997) Horizontal-to-vertical spectrum ratio of earthquake ground motion for site characterization. *Earthquake Eng Struct Dyn* 26:671–689
- Zafarani H, Noorzad A, Ansari A, Bargi K (2009) Stochastic modeling of Iranian earthquakes and estimation of ground motion for future earthquakes in Greater Tehran. *Soil Dyn Earthq Eng* 29(4):722–741
- Zafarani H, Hassani B, Ansari A (2012) Estimation of earthquake parameters in the Alborz seismic zone, Iran using generalized inversion method. *Soil Dyn Earthq Eng* 42:197–218
- Zare M, Bard PY, Ghafory-Ashtiany M (1999) Site characterizations for the Iranian strong motion network. *Soil Dyn Earthquake Eng* 18:101–123
- Zarrineghbal A, Zafarani H, Rahimian M (2021) Towards an Iranian national risk-targeted model for seismic hazard mapping. *Soil Dyn Earthq Eng*. <https://doi.org/10.1016/j.soildyn.2020.106495>
- Zhao JX, Irikura K, Zhang J, Fukushima Y, Somerville PG, Asano A (2006) An empirical site classification method for strong-motion stations in Japan using H/V response spectral ratio. *Bull Seism Soc Am* 96:914–925
- Zhao JX, Irikura K, Zhang J, Fukushima Y, Somerville PG, Saiki T, et al (2004) Site classification for strong motion stations in Japan using H/V response spectral ratio. In: 13th World conference of earthquake engineering. Vancouver, BC, Canada, 2004. Paper no 1278
- Zhifeng Hu (2022) Kim B Olsen, Steven M Day, 0–5 Hz deterministic 3-D ground motion simulations for the 2014 La Habra California, Earthquake. *Geophys J Int* 230(3):2162–2182

**Publisher’s note** Springer Nature remains neutral with regard to jurisdictional claims in published maps and institutional affiliations.

Springer Nature or its licensor (e.g. a society or other partner) holds exclusive rights to this article under a publishing agreement with the author(s) or other rightsholder(s); author self-archiving of the accepted manuscript version of this article is solely governed by the terms of such publishing agreement and applicable law.